

# Chapter 1

## Supplementary Theory

---

### 1.1 Mie Theory

---

Mie theory [1] is used to calculate the scattering cross section of MNPs outside of the quasistatic regime. In Mie theory, solutions for EM scattering from a spherical particle are given as a superposition of spherical waves generated by electrical and magnetic multipoles. The amplitude of each electrical and magnetic multipole of order  $l$  is given by,

$$a_l = \frac{M\Psi_l(Mx)\Psi'_l(x) - \Psi'_l(Mx)\Psi_l(x)}{M\Psi_l(Mx)\xi'_l(x) - \Psi'_l(Mx)\xi_l(x)}, \quad (1.1a)$$

$$b_l = \frac{\Psi_l(Mx)\Psi'_l(x) - M\Psi'_l(Mx)\Psi_l(x)}{\Psi_l(Mx)\xi'_l(x) - M\Psi'_l(Mx)\xi_l(x)}, \quad (1.1b)$$

respectively, where  $x = n\pi D/\lambda$  is the size parameter,  $n$  is the refractive index,  $D$  is the particle diameter,  $M = (\varepsilon/\varepsilon_d)^2$ ,  $\Psi_l$  and  $\xi_l$  are  $l$ -order Riccati-Bessel and Hankel functions, respectively, and  $l$  is the degree of spherical harmonic (multipolar distribution). The extinction and scattering cross sections are then calculated using the multipolar expansion,

$$\sigma_{\text{ext}} = \frac{2\pi}{k^2} \sum_{l=1}^{\infty} (2l+1) \text{Re}[a_l + b_l], \quad (1.2a)$$

$$\sigma_{\text{scat}} = \frac{2\pi}{k^2} \sum_{l=1}^{\infty} (2l+1) (|a_l|^2 + |b_l|^2). \quad (1.2b)$$

The results of scattering calculations for AuNPs are shown in the main text.

### 1.2 Quantum Charge Transport

---

One of main discussions of this work is the effect of quantum charge transport on plasmon coupling. Both quantum tunnelling and ballistic transport are qualitatively described in the

main text for simplicity. The following section shows the relevant mathematical derivations of the simplest cases of quantum tunnelling and ballistic transport.

### 1.2.1 Quantum Electron Tunnelling

Electron tunnelling is predicted by the time-independent Schrödinger equation for an electron impinging upon a simple rectangular potential barrier, in which,

$$-\frac{\hbar^2}{2m^*} \frac{d^2\psi(x)}{dx^2} + V(x)\psi(x) = E\psi(x), \quad (1.3)$$

where  $m^*$  is the effective electron mass,  $V(x)$  is the local potential (either zero or the barrier height  $V_0$  depending on the region) and  $E$  is the electron energy. A propagating electron incident on the barrier with a wavefunction  $\psi = e^{ikx}$  has an energy given by,

$$E = \frac{\hbar^2 k^2}{2m^*}. \quad (1.4)$$

Inside the barrier the wavefunction decays as  $e^{-\beta x}$  where,

$$\beta^2 = \frac{2m^*}{\hbar^2}(V_0 - E). \quad (1.5)$$

The transmission probability of the electron passing through the barrier is calculated in the WKB approximation as [2],

$$T(E) = \exp \left\{ -2 \int_0^{d_0} \beta(x) dx \right\}, \quad (1.6)$$

$$= \exp \left\{ -2 \left[ \frac{2m^*}{\hbar^2} (V_0 - E) \right]^{\frac{1}{2}} d_0 \right\}, \quad (1.7)$$

where  $d_0$  is the barrier width. Though assuming a simple rectangular barrier, Eq. 1.7 shows the characteristic exponential dependence of electron tunnelling.

### 1.2.2 Ballistic Conduction

A 1D constriction between two charge reservoirs of length  $L$  and width  $W$  can be described as either diffusive if  $l, l_\phi \ll L, W$ , ballistic if  $l, l_\phi \gg L, W$ , or quasi-ballistic if inbetween, where  $l$  and  $l_\phi$  are the mean free path and phase coherence length, respectively. Conductance in the diffusive regime is as classically expected,  $G = \sigma_{2D} W/L$ . In the ballistic regime, however, it

inherits quantum properties as is thus given by the Landauer formula,

$$G = \frac{2e^2}{h} T(E_F), \quad (1.8)$$

where  $T(E_F)$  is the transmission coefficient of an electron at the Fermi level. This is derived from the current flowing through a barrier between two biased reservoirs, whereby the Fermi levels are related via  $E_{F,L} - E_{F,R} = eV$ . The leftwards current through a barrier is given by,

$$I_L = 2e \int_0^\infty f(E(k), E_{F,L}) v(k) T(k) \frac{dk}{2\pi}, \quad (1.9)$$

where  $f(E, E_F)$  is the Fermi-Dirac function and the wavevector of an electron can be related to its energy via  $dE = \hbar v dk$ . Converting Eq. 1.9 to an energy basis and adding the rightwards current yields,

$$I_L = \frac{2e}{h} \int_{E_L}^\infty [f(E(k), E_{F,L}) - f(E(k), E_{F,R})] T(E) dE. \quad (1.10)$$

In the small bias limit<sup>1</sup> the Fermi-Dirac function is expanded as a Taylor series into,

$$f(E(k), E_{F,L}) - f(E(k), E_{F,R}) \approx eV \frac{\delta f(E(k), E_F)}{\delta E_F}. \quad (1.11)$$

Substituting this into Eq. 1.10 yields the integral,

$$I_L = \frac{2e^2 V}{h} \int_{E_L}^\infty \left[ -\frac{\delta f}{\delta E} \right] T(E) dE. \quad (1.12)$$

At low temperatures  $\delta f/\delta E \rightarrow \delta(E - E_F)$  and the integral evaluates to,

$$I_L = \frac{2e^2 V}{h} T(E_F), \quad (1.13)$$

from which the conductance  $G = I/V$  is derived to be,

$$G = \frac{2e^2}{h} T(E_F). \quad (1.14)$$

With the barrier still in place this corresponds to a tunnelling conductance with  $T(E_F) < 1$ . The point at which the barrier disappears ( $E_{barrier} = E_F$ ) gives rise to  $T(E) = 1$  and opens up a single quantised conductance channel. Adding additional  $n$  sub-bands into the constriction continues to increase the conductance by its quantum,  $2e^2/h$ , and thus the conductance of a

---

<sup>1</sup>Large biases are ignored

1D *conductive* junction can be expressed as,

$$G = \frac{2e^2}{h}n. \quad (1.15)$$

## Chapter 2

# Supplementary Experimental Details

---

### 2.1 Supplementary Optical Details

---

Features, design justifications and optical theory not essential to the main text are detailed here, including notes on reimaging, choice of objectives and polarisation optimisation. The concept of reimaging, and its effect on beam alignment, is shown in Figure 2.1. The ray diagrams show that the beam position in the focus can be adjusted by changing the angle of a mirror placed in the Fourier plane (in the case of the microscope the mirror directly after the DF stop). The shape of the beam, dictated by its angular distribution in Fourier space, is controlled by tilting a mirror in a focal plane (the mirror in the focus of the reimaging arm). The two mirrors provide independent control over the two main beam properties.

The choice of objective was determined by the overall range over which a reference spectrum from a Ag mirror is valid. Two long working distance objectives suitable for single nanostructure spectroscopy were characterised for use in the microscope: a VIS and an IR objective. The raw reflectance spectrum of the supercontinuum laser measured using each objective is shown in Figure 2.2. The short wavelength cut-off at 480 nm is due to the supercontinuum laser. The VIS objective clearly outperforms the IR objective below 625 nm, though both objective counts are large enough to maintain a good reference signal. Overall, references using the VIS objective only extend marginally more below 500 nm. However, the

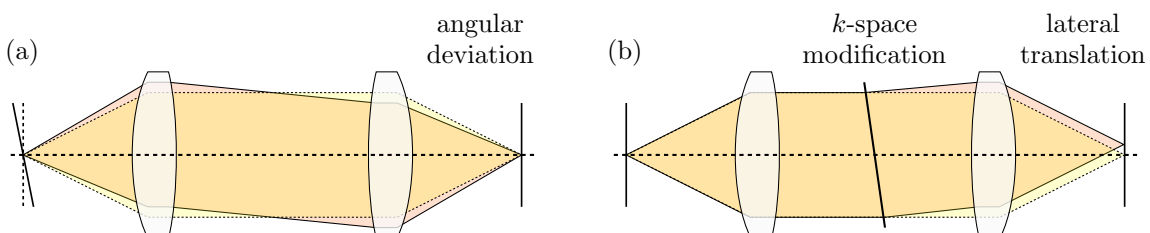
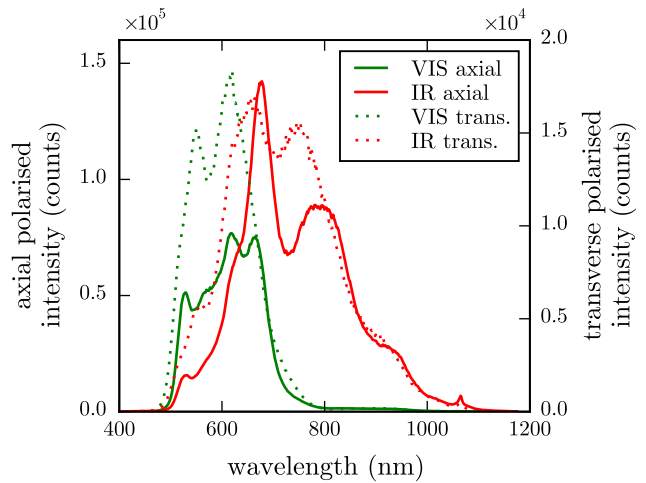


**Figure 2.1: Concept of reimaging for beam alignment.** (a) Adjusting the angle of the beam in a focal plane does not change the position of the focus in the image (front focal) plane but changes the position in the Fourier (back focal) plane. (b) Adjusting the angle of the beam in a Fourier plane translates the position of the beam in the image plane without changing its angular components.

**Figure 2.2: Spectral comparison between VIS and IR objectives.** The VIS objective is an Olympus  $100\times 0.9$  NA MPlan BD dark-field objective whereas the IR objective is an Olympus  $100\times 0.8$  NA MPlan bright-field objective.



700 nm cut-off of the VIS objective means that it is not suitable for spectra in the NIR with referencing only valid up until 900 nm whereas the IR objective extends to 1100 nm. The gain in spectral range means that the IR objective is chosen despite its lack of dark-field illumination for imaging.

Consideration was given when designing the optical layout to account for intensity differences in each linear polarisation. Reflection and transmission of an EM wave incident on an interface between two refractive media at an angle is governed by the Fresnel equations [3]. As shown in Figure 2.3, there is a large difference in reflectance between linear polarisations at higher angles of incidence. The microscope is designed such that the *s*-polarisation corresponds to light polarised along the tip axis, maximising its transmission to the spectrometers. Leakage of the *s*-polarisation into the weaker *p*-polarisation signal at the polarising beam-splitter limits current polarisation resolved measurements.

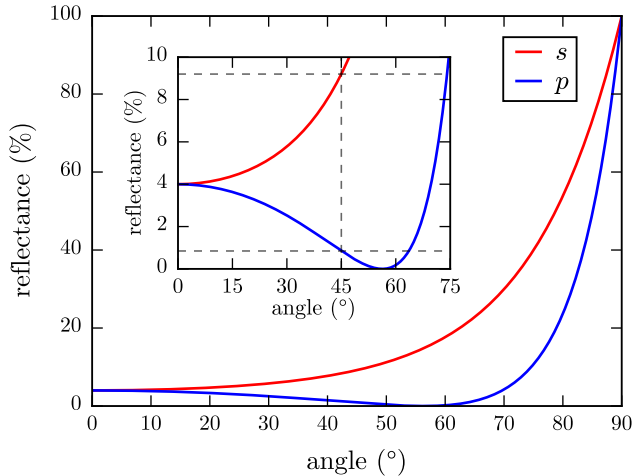


**Figure 2.3: Reflectance as a function of angle of incidence for glass-air interface.** Reflective is calculated from the fresnel coefficients. The refractive index of glass is assumed to be  $n = 1.5$ . The inset shows a zoomed segment at low reflectances.

## 2.2 Supplementary Electronics

The schematic circuitry of the microscope electronics is shown in Figure 2.4, corresponding to the simpler block diagram shown in the main text.

## 2.3 Software Lock-In Derivation

To lock into only the signal component at the reference frequency  $\omega_r$  a reference wave needs to be computed. The first step in the lock-in process is to mathematically construct a single frequency waveform at the correct harmonic using the supplied reference signal. The reference signal is typically of the form  $A \sin(\omega_{rs}t + \phi_r)$ , but the algorithm will also work with any periodic function since it triggers off a rising position edge. When  $\sin(\theta) = 0$  and the gradient is positive ( $\cos(\theta) = 1$ )  $\theta = 2n\pi$ . Hence the rising edge trigger points  $t_i$  occur at,

$$\theta = \omega_{rs}t_i + \phi_r = 2n\pi. \quad (2.1)$$

Trigger times are fitted against the number of triggers (number of periods) since the start of the signal using,

$$t_i = \frac{1}{\omega_{rs}}(2n\pi - \phi_r) = \frac{2\pi}{\omega_{rs}}n - \frac{\phi_r}{\omega_{rs}}. \quad (2.2)$$

A complex reference wave of the form  $e^{ih(\omega_{rs}t + \phi_r)}$ , where  $h$  is the harmonic of the reference frequency  $\omega_{rs}$  required to lock into the frequency  $\omega_r$ , is constructed from the  $t_i = mn + c$  fit using,

$$\omega_{rs} = \frac{2\pi}{m}, \quad (2.3)$$

$$\phi_r = \frac{mc}{2\pi}. \quad (2.4)$$

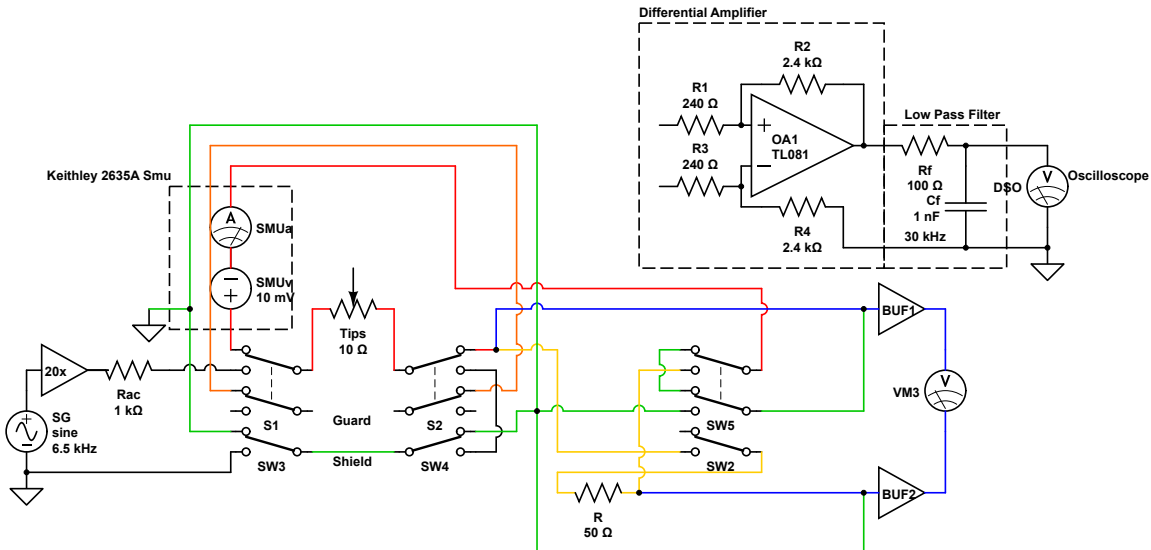


**Figure 2.4: Schematic of the electrical measurement circuit.** The central routing box allows switching between a.c. and d.c. circuits and low-and high-bandwidth d.c. measurements. The a.c. circuit is used to align two AFM probes together while the d.c. circuit is used to measure spatially dependent signals from the gap between two AFM probes.

The frequency component of the signal at  $\omega_r = h\omega_{rs}$  can be extracted using Fourier analysis,

$$Z_s(\omega_r) = \frac{2}{t} \int_0^t Z_s(t) e^{-ih(\omega_{rs}t + \phi_r)} dt. \quad (2.5)$$

Discretising this not a programmable form results in,

$$Z_s(\omega_r) = \frac{2}{n} \sum_0^n Z_s(t_n) e^{-ih(\omega_{rs}t_n + \phi_r)} \quad (2.6)$$

where  $\text{Re}[Z_s(\omega_r)]$  and  $\text{Im}[Z_s(\omega_r)]$  are the  $x$  and  $y$  of the signal component at  $\omega_r$ , respectively. Polar coordinates of amplitude and phase are retrieved using the coordinate transforms,

$$r = \sqrt{x^2 + y^2}, \quad (2.7)$$

$$\phi = \tan^{-1}(y/x). \quad (2.8)$$

## 2.4 Capacitive Alignment Model Derivation

---

The equation of motion for the dual-tip system is derived in the main text as,

$$m_1 \frac{d^2 z_1}{dt^2} + \beta_{01}^z \frac{dz_1}{dt} + k_{01}^z (z_1 - d_0) = \left( \frac{-\varepsilon_0 A_{ov} V_0^2}{4z_1^2} \right) [1 + \cos(\omega_p t)]. \quad (2.9)$$

Expressing Eq. 2.9 in terms of  $z_r = z - d_0$  yields,

$$m_1 \frac{d^2 z_r}{dt^2} + \beta_{01}^z \frac{dz_r}{dt} + k_{01}^z z_r = \left( \frac{-\varepsilon_0 A_{ov} V_0^2}{4(z_r + d_0)^2} \right) [1 + \cos(\omega_p t)], \quad (2.10)$$

and enables further simplification via approximation. Assuming that  $z_r \ll d_0$  the right hand side of Eq. 2.10 can be taken to first order using a Taylor series,<sup>1</sup>

$$m_1 \frac{d^2 z_r}{dt^2} + \beta_{01}^z \frac{dz_r}{dt} + k_{e1}^z z_r \simeq \left( \frac{-\varepsilon_0 A_{ov} V_0^2}{4d_0^2} \right) [1 + \cos(\omega_p t)], \quad (2.11)$$

where,

$$k_{e1}^z = k_{01}^z - \left( \frac{\varepsilon_0 A_{ov} V_0^2}{2d_0^3} \right) [1 + \cos(\omega_p t)]. \quad (2.12)$$

This effective spring constant  $k_{e1}^z$  does not cause parametric mixing as it oscillates at  $\omega_p$  therefore its effect can be averaged out over time resulting in  $\langle k_{e1}^z \rangle = k_{01}^z - \varepsilon_0 A_{ov} V_0^2 / 2d_0^3$ . The

---

<sup>1</sup> $F(z_r) = F(0) + \frac{dF(z_r)}{dz_r} \Big|_0 z_r = \left( \frac{-\varepsilon_0 A_{ov} V_0^2}{4} \right) [1 + \cos(\omega_p t)] \left( \frac{1}{d_0^2} - \frac{2z_r}{d_0^3} \right)$

EoM is then once again approximated to,

$$m_1 \frac{d^2 z_r}{dt^2} + \beta_{01}^z \frac{dz_r}{dt} + \langle k_{e1}^z \rangle z_r \simeq \left( \frac{-\varepsilon_0 A_{ov} V_0^2}{4d_0^2} \right) [1 + \cos(\omega_p t)], \quad (2.13)$$

Defining the constant  $q$  as,

$$q = \left( \frac{-\varepsilon_0 A_{ov} V_0^2}{4d_0^3} \right), \quad (2.14)$$

the effective spring constant can be expressed as,

$$k_{e1}^z = k_{01}^z + 2q [1 + \cos(\omega_p t)], \quad (2.15)$$

$$\langle k_{e1}^z \rangle = k_{01}^z + 2q, \quad (2.16)$$

and the EOM can be again rewritten in the form,

$$m_1 \ddot{z}_r + \beta_{01}^z \dot{z}_r + [\langle k_{e1}^z \rangle + 2q \cos(\omega_p t)] z_r - q [1 + \cos(\omega_p t)] d_0 \simeq 0, \quad (2.17)$$

Equation Eq. 2.17 is of the form of the driven damped Mathieu equation,

$$\ddot{z} + 2\kappa \dot{z} + [a - 2q \cos(2t)] z = F(t), \quad (2.18)$$

and has solutions in the limit of small oscillations of [4],

$$z_1 \approx d_0 - |z_1^{off}| - z_{m1} \cos(\omega_p t + \varphi_1) \quad (2.19)$$

where

$$z_1^{off} \approx \frac{\varepsilon_0 A_{ov} V_0^2}{4d_0^2 \langle k_{e1}^z \rangle}, \quad (2.20a)$$

$$z_{m1} \approx \frac{\varepsilon_0 A_{ov} V_0^2}{4d_0^2 \sqrt{(\langle k_{e1}^z \rangle - m_1 \omega_p^2)^2 + (\beta_{01}^z \omega_p)^2}}, \quad (2.20b)$$

$$\varphi_1 \approx \tan^{-1} \left( \frac{\beta_{01}^z \omega_p}{\langle k_{e1}^z \rangle - m_1 \omega_p^2} \right). \quad (2.20c)$$

## Chapter 3

# Fast Spectroscopy of Plasmonic Dimer Make/Break Junctions

---

One of the aspects of the microscope platform not discussed in the main text is the capability for fast spectroscopy with  $10\text{ }\mu\text{s}$  resolution. This was developed in order to measure the initial contact dynamics of plasmonic tip dimers as they come into conductive contact, along with the plasmonics of break junctions formed between the two Au surfaces in a touching tip dimer. Mechanically controllable break junctions (MCBJs) similar to the Au contact formed between tips are well documented and have formed the basis of quantised conductance studies in 3D systems at room temperature (as opposed to the original 2DEG systems) [5–15].

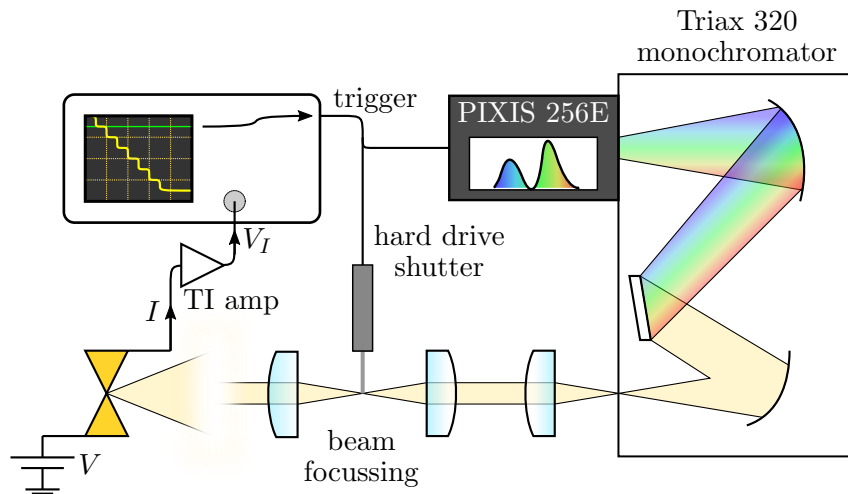


**Figure 3.1: Diagram of the fast spectroscopy setup.** The setup consists of a custom shutter, built from a disassembled hard drive, and a monochromator-CCD pair. Kinetics acquisition on the CCD, along with the shutter mechanism, is triggered by fast electrical signals from the tips which are measured on the oscilloscope.

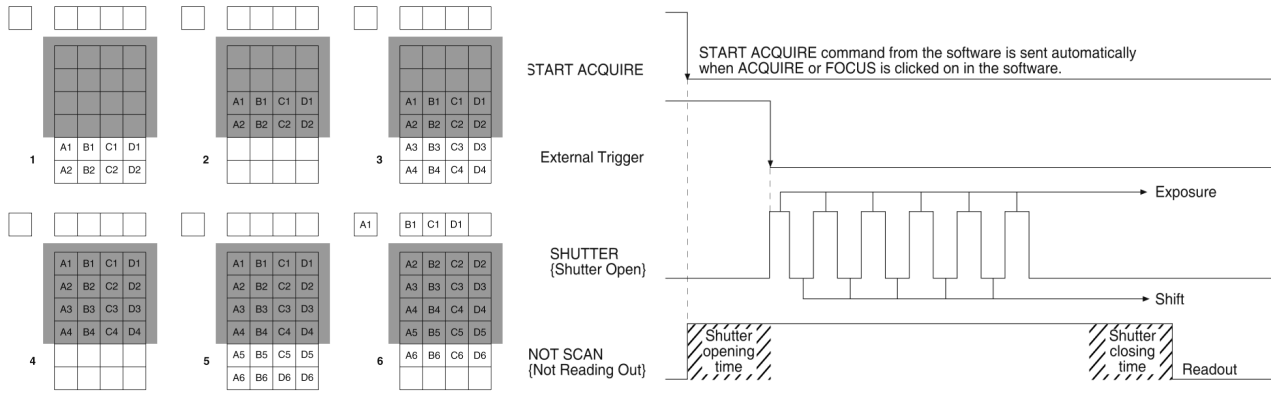


**Figure 3.2: Diagram showing kinetics mode acquisition on the CCD.** An exposed region of the CCD is shuffled into a mechanically or optically masked region. Once the whole CCD has been exposed the image is read out. This acquisition process, along with the opening of the fast shutter, is triggered by an external TTL pulse from an oscilloscope. These images are taken from the Princeton Instruments PIXIS CCD manual.

### 3.1 Experimental Setup

The experimental setup for fast spectroscopy is shown in Figure 3.1. Collimated scattered light from the tips is focussed down onto the end of the shutter blade and then, with the shutter open, reimaged onto the entrance slit of a monochromator (Horiba Yvon Jobin Triax 320). The monochromator is paired with a CCD supporting a kinetics readout mode (Princeton Instruments PIXIS 256E), wherein charge is shuffled down the active CCD area after the single top-most line of pixels is exposed to produce a time-series of spectra. The time interval recorded during time-resolved spectroscopy is given by,

$$t_{\text{range}} = 256(t_{\text{exposure}} + t_{\text{shift}}), \quad (3.1)$$

where  $t_{\text{exposure}}$  is the exposure period of each row of pixels and  $t_{\text{shift}}$  is the time taken to shift all pixels by one row. The shuffle speed is fast ( $9.2 \mu\text{s}$ ) compared with the readout time meaning it is possible to obtain resolutions around  $10 \mu\text{s}$  with the complete image readout only once the kinetics process has completed. Kinetics acquisition is therefore good for measuring short-lived, single-shot events, similar in application to a streak camera. A coarse,  $150 \text{ lines mm}^{-1}$  diffraction grating is chosen to disperse the visible spectrum along the top row of the CCD. The fast spectroscopy path from its initial split off point at the beamsplitter is completely tubed to reduce any background noise incident on the sensitive CCD, with an opening only to place the shutter in the beam.

The kinetics sequence is armed at the start of each experiment, waiting for a trigger signal to begin acquisition. To improve the activation time upon receiving the trigger signal

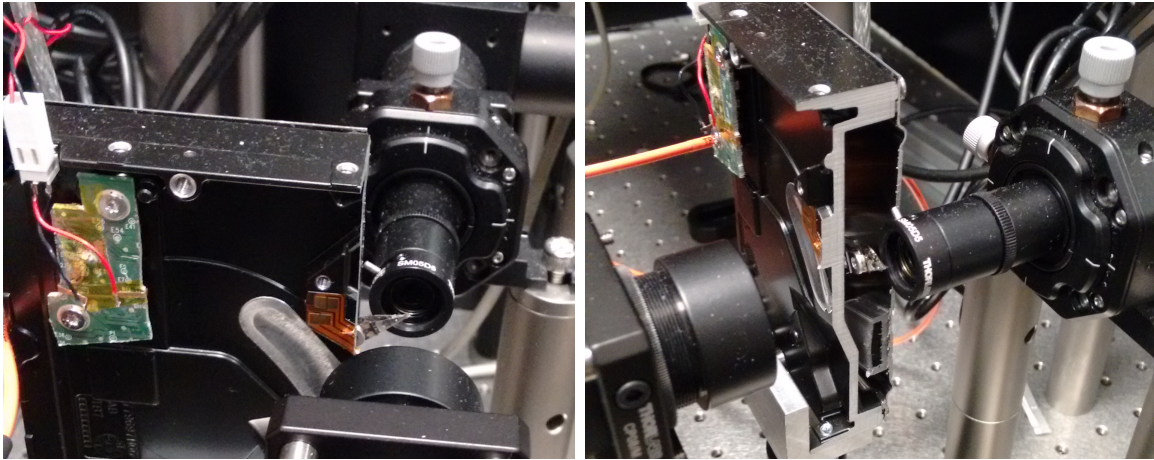


**Figure 3.3: Images of the hard drive shutter.** The shutter works by passing a current through the hard drive voice coil, generating a magnetic field which quickly moves the read head via a Lorentz force. This functions as a shutter blade. The shutter blade is placed in the focus between two lenses in order to uncover the focussed beam spot in the shortest possible time. Rise times in this configuration are around 300  $\mu$ s.

non-essential CCD procedures, such as continuous cleaning, are deactivated. The CCD is protected from pre-sequence overexposure by a custom-built fast shutter, constructed using the read head from a disassembled 3.5" computer hard-drive, shown in Figure 3.3. The hard drive is mounted onto a 3D translation stage and the shutter blade is aligned in the focus of the scattered light such that the time taken to uncover the beam is minimised. Regular shutters are limited to 8 ms opening times due to solenoid delay and thus the majority of a short,  $\sim$ 10 ms make/break junction event would be missed. Use of the hard-drive voice coil mechanism enables shutter open times of around 300  $\mu$ s, as confirmed using both CCD and photodiode measurements. Currents to the voice coil and their trigger mechanism are provided by an Arduino microcontroller with a motor driver circuit, enabling up to 2 A of current. The fast trigger mechanism is enabled by directly addressing each bit of the circuit and bypassing the standard Arduino functions. These kinds of shutters have been previously developed [16, 17] though not before with the simplicity of using Arduino circuit boards and programming.

The trigger signal to the CCD and shutter is provided by the oscilloscope. The oscilloscope is set to trigger once the tip junction conductance either rises above  $1G_0$  or falls below  $10G_0$ . As tips come into contact or as the contact area between pulled tips is reduced the number of conductance channels discretely changes by  $G_0$ . The trigger signal synchronises the electronic and spectral measurements to facilitate correlation comparisons. The current limiting resistor described in chapter ?? was installed primarily to prevent the amplifiers feeding the oscilloscope from overloading, thus causing the break junction event to be missed in the time taken for the amplifiers to reset. To ensure correct triggering and optimum electronic measurements, electrical signals passing through the high bandwidth d.c. circuit are cleaned up

using low pass filters and a multi-stage (transimpedance) amplification process to maintain a 1 MHz bandwidth at a total gain between  $10^4$ – $10^5$ .

## 3.2 Performance and Issues in Tip Dimer Scanning Experiments

Both make and break contact events typically last no more than 10 ms in the current system, often occurring more on a 100  $\mu$ s–1 ms time scale. The kinetics mode has a minimum acquisition time of 2.56 ms with a maximum 10  $\mu$ s single spectrum time resolution set by the pixel shift time. The system is trialled using a reflected supercontinuum laser beam with an additional 10  $\mu$ s exposure per row of pixels to give a 5 ms measurement, shown in Figure 3.4. The beam is chopped and measured on a photodiode to show the system is working as expected. Similar tests were performed with an electronically modulated diode laser to determine the time resolution of measurements.

Figure 3.5 shows an example of a conductance traced measured on a break junction between two tips. The traces shows that as the tip contact breaks, the conductance drops in units of  $G_0$ . Under these circumstances the CTP modes sustained by the tip dimer are expected to undergo a redshift with decreasing conductance (ideally in discrete quantised steps). Make junctions, as opposed to break junctions, showed more success in tips since the jump into contact is generally a single high quality event whereas in break junctions the forces holding

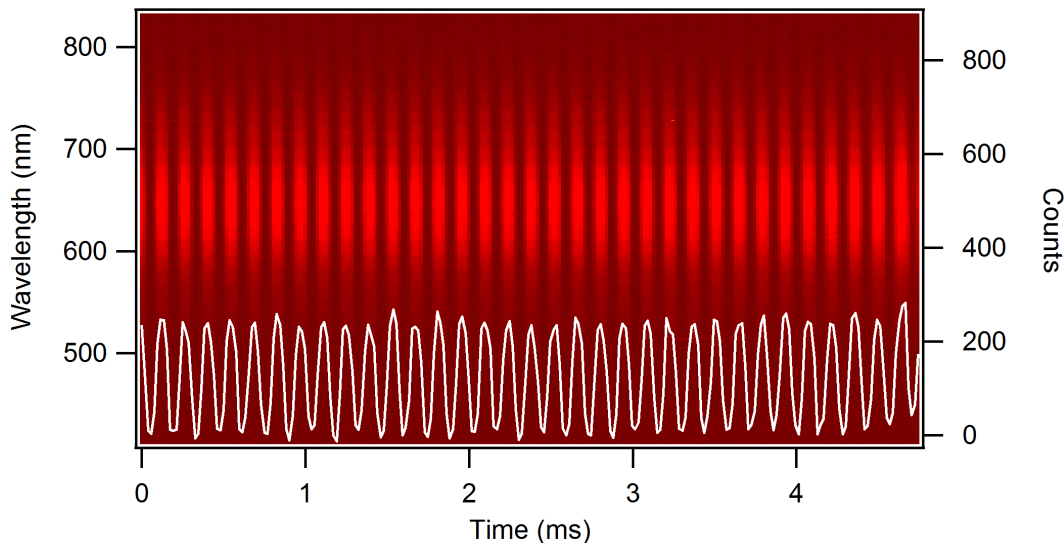


**Figure 3.4: Testing of kinetics mode acquisition.** A reflected supercontinuum beam is chopped and measured both with kinetics mode on the CCD and by a photodiode on the oscilloscope. Oscillations in the beam at the chopping frequency are clearly seen in both the spectral image and the superimposed photodiode output over a 5 ms time period.

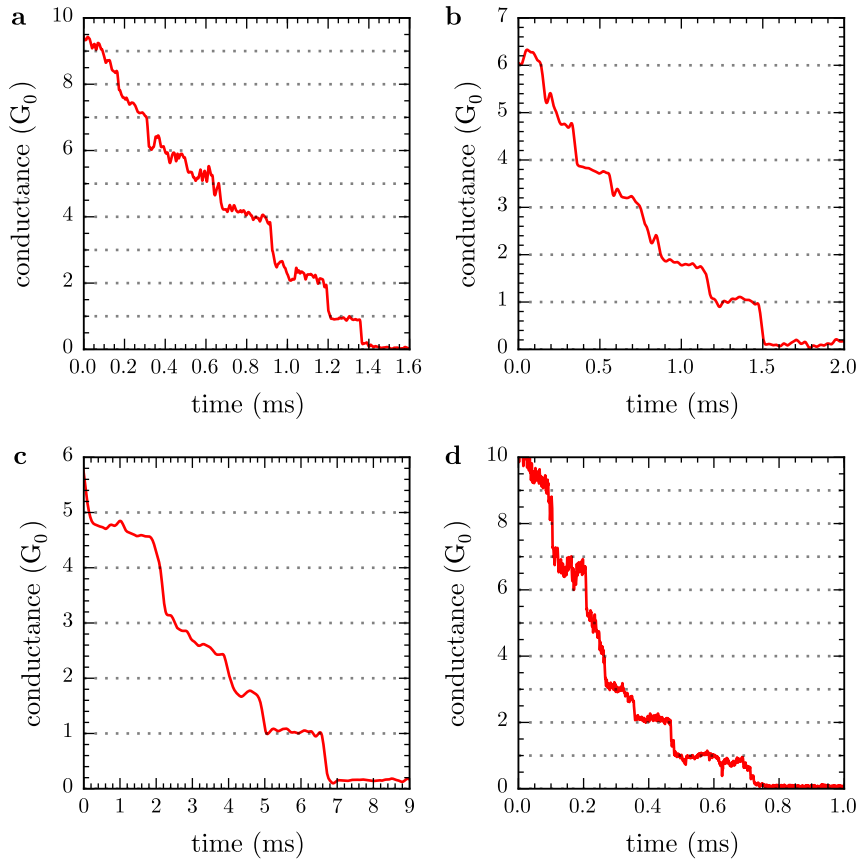


**Figure 3.5: Examples of fast conductance measurements on tip dimer break junctions.** During the break the contact conductance drops in units of  $G_0$  until the last atom-atom contact breaks and tips separate.

the tip together and the flexibility of the cantilevers causes issues. Tips often exhibit multiple breaks or changes in conductance as the junction vibrates with the final break occurring only once the gap adhesion forces are overcome. Given the strength of the average tip adhesion (and that it often causes the ball to break from the tip apex) the large amount of pulling force applied to the cantilever leads to a very quick sub- $\mu$ s break event. This is not possible to measure in the given system. Although the make contact event is typically higher quality it is far more difficult to trigger due to operating near the noise floor, often meaning that the  $1G_0$  level is too low to reliably observe.

Though the fast spectroscopy system was engaged in every scan the method provided no useable results. Spectral images contained no detectable signals, as shown in Figure 3.6, due to the short exposure times and low supercontinuum laser powers used to prevent damage to tips. Eventually the  $G_0$ -level conductance data was measured using a slow, controlled make junction in a standard spatial scan (shown in ??b). For this technique to become useful the length of the break or make contact event needs to be lengthened in order to increase the exposure time per row of pixels on the CCD. This could be achieved through more control of the tip position, i.e. by using stiff tips in a low humidity environment to minimise adhesion and more

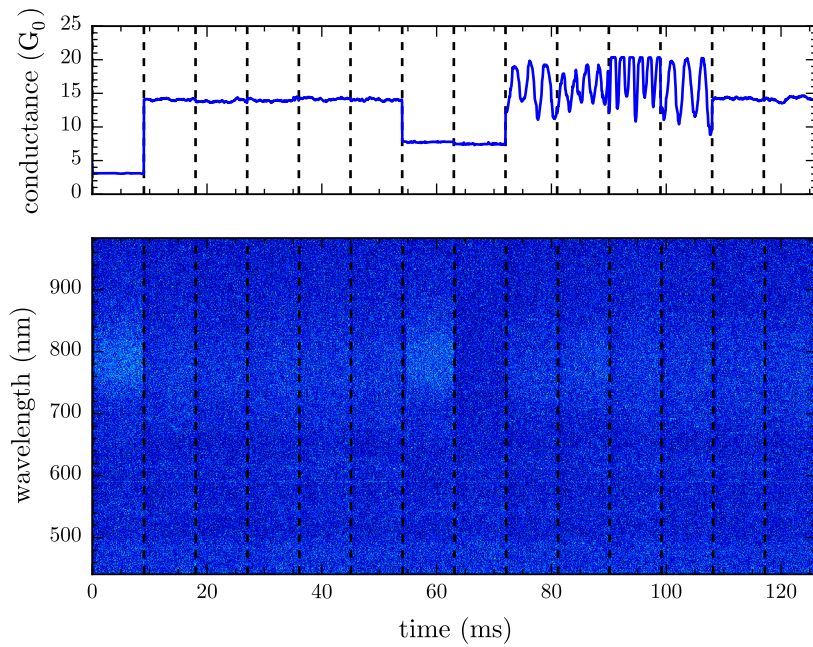


**Figure 3.6:** A representative fast scanning measurement from a plasmonic tip dimer. No signal is detectable with such small exposures per spectrum at acceptable power levels.

controllably break the contact without significantly bending the cantilever. Alternatively, the increased robustness of the electrochemically fabricated plasmonic tips means increased focal intensities could be sustained. By leveraging both of these suggestions in the future, plasmonic MCBJs could be realised as a means of studying conductance at optical frequencies.